WILEY | Hindawi

Research Article

Cu$_3$P Nanoarrays Derived from 7,7,8,8-Tetracyanoquinodimethane for High-Rate Electrocatalytic Oxygen Reactions of Lithium-Oxygen Batteries

Chan Ho Kim, Myeong-Chang Sung, Byoungjoon Hwang, and Dong-Wan Kim [ORCID]

School of Civil, Environmental and Architectural Engineering, Korea University, Seoul 02841, Republic of Korea

Correspondence should be addressed to Dong-Wan Kim; dwkim1@korea.ac.kr

Efficient electrocatalysis at the cathode is crucial for addressing the challenges faced by lithium-oxygen batteries (LOBs), including limited stability and low-rate capability. To develop an efficient cathode for aprotic LOBs, self-supported copper phosphide nanoarrays on carbon cloth are prepared at different heating rates via a phosphidation process using CuTCNQ nanoarrays. Different ramping rates have effects on particle size and intrinsic interaction, which in turn affect their catalytic properties. When phosphidation is carried out at a slow rate, it results in the formation of smaller, evenly distributed Cu$_3$P particles on the nanoarrays (SG-Cu$_3$P NAs/CC) compared to fast rate phosphidation (FG-Cu$_3$P NAs/CC). As a result, SG-Cu$_3$P NAs/CC exhibits lower resistance and a higher concentration of active sites than FG-Cu$_3$P NAs/CC. The SG-Cu$_3$P NAs/CC demonstrates LOBs with a low overpotential of 1.51 V at a high current rate of 1 mA cm^{-2} and a long cycle life of 115 cycles at 0.1 mA cm^{-2}. The in situ Raman spectroscopy supports that Li$_2$O$_2$ is uniformly formed and decomposed on the SG-Cu$_3$P NAs/CC surface. This study provides a compelling approach for the precise fabrication and analysis of binder-free, self-supported copper phosphides as highly efficient and stable materials for bifunctional oxygen electrocatalysis.

1. Introduction

Various types of battery systems have been developed to improve the disadvantages of lithium-ion batteries [1–6]. LOBs have gained considerable prominence owing to their substantial theoretical energy density resulting from the generation of Li$_2$O$_2$ products (~3500 Wh kg^{-1}) [7–10]. Nonetheless, the practical utility of LOBs is encumbered by the slow kinetics and suboptimal energy efficiency during the discharge and charge processes, encompassing the oxygen reduction reaction (ORR) and oxygen evolution reaction (OER) [11, 12]. These reactions involve both the formation and decomposition of Li$_2$O$_2$ products. The distinct characteristics of Li$_2$O$_2$, notably its insulating and insoluble nature, impede electron and charge transfer, leading to poor cycling performance [13].

Various noble metal catalysts, including platinum, gold, silver, and ruthenium, have been extensively studied for addressing this challenge [14–17]. Consequently, the focus only lies in developing a catalyst with exceptional activity that can reduce the energy barriers required for the formation and decomposition of Li$_2$O$_2$ products at the cathode. However, noble metal catalysts are not suitable for practical applications because of scarcity, high price, and unsatisfying stability. This remains a formidable impediment to the advancement of these LOBs. In recent years, research into highly catalytic, earth-abundant materials has unveiled several alternative materials, including transition-metal moieties (oxides, dichalcogenides, carbides, nitrides, etc.) and even metal-free compounds [18–27]. Furthermore, numerous combinations of catalysts based on cobalt, iron, nickel, copper oxides/hydroxides, and carbon-based materials have been explored as prospective bifunctional oxygen catalysts [28–33].

Transition-metal phosphides are particularly promising and competitive candidates for the electrocatalytic ORR and OER owing to their cost-effectiveness, tunable composition, and favorable electrical conductivity [34–36]. For instance, Kondori et al. introduced highly active Mo$_3$P

nanoparticles as HER catalysts, and the Mo_3P nanoparticles were applied as ORR and OER catalysts of LOBs. Throughout cycling, the formation of a stable MoO monolayer on the Mo-terminated surface sites led to enhanced catalytic performance [37, 38]. Furthermore, Zhang et al. employed urchin-like CoP microspheres as catalysts for the ORR and OER in LOBs, underscoring their intrinsic excellence [35].

Other strategies have focused on creating conductive heterostructures to augment catalytic activity that has gained attention. The multiphase nanointerface with a built-in electric field has been shown to facilitate interfacial charge transfer, thereby significantly influencing the adsorption of reactants and intermediates during the electrocatalytic process [29, 30]. Cooperative electron transfer interactions between different metal species can change the electronic state of the metal atom center, optimizing the adsorption strength of crucial intermediates. For example, Lv et al. synthesized the $Ni_2P@Cu_3P$/CF heterojunction, ascribing the enhanced conductivity to the heterointerfaces [39]. These interfaces controlled the bonding energy in both Cu–P and Ni-P, thereby promoting electron migration from Cu_3P species towards Ni_2P.

The application of metal-organic frameworks (MOFs) stands out as a robust approach for nitrogen doping to achieve improved electroconductivity [19, 26, 40–42]. MOFs also offer the distinct advantages of uniform catalyst dispersion and facile control over the catalyst morphology, including the engineering of one-dimensional structures. For instance, coordination polymers incorporating 7,7,8,8-tetracyanoquinodimethane (TCNQ) have been applied in morphology-controlled catalyst synthesis, yielding a diverse array of structures, including wires and cubes. TCNQ is not only an excellent carbon source but also incorporates nitrogen within its molecular structure, introducing defects that enhance the conductivity of the material [43, 44]. Recently, a nanoarray with enhanced catalytic performance was developed by utilizing TCNQ. Yoo et al. exploited uniform TCNQ-based CuTCNQ nanorods in fabricating Ru-doped CuO nanorods and demonstrated their feasibility as bifunctional electrocatalysts [32].

For electrochemical analyses and practical use, the target catalysts must be immobilized on electrode surfaces using a polymer binder such as carboxymethyl cellulose or poly(1,1,2,2-tetrafluoroethylene). However, this procedure is time-intensive, and the polymer binder can occlude the active sites of the catalyst and hinder molecular diffusion, thereby reducing the effective catalytic activity. This problem can be effectively addressed by conceptualizing binder-free cathodes for oxygen reactions, in which the active phases are directly grown on current-collecting substrates. Self-supported arrays featuring one-dimensional (1D) nanostructures on current collectors are especially intriguing due to their advantageous directional electron-transport properties. Uniform 1D structures offer ample room and active sites for ion exchange, thus facilitating the rapid transport of O_2 in the axial direction [45]. Sung et al. introduced homogeneously dispersed defects into perovskite $La_{0.8}Sr_{0.2}VO_3$ nanofibers, achieving uniform deposition of Li_2O_2 along the nanofiber surface during the discharge process [46].

Herein, novel self-supported Cu_3P nanoarrays on porous carbon cloth are synthesized through a straightforward phosphidation process using CuTCNQ nanoarrays as a precursor. Cu_3P has been studied as an aqueous OER catalyst, but research as a lithium-air battery catalyst has not yet been conducted [47]. We firstly reported Cu_3P cathode catalysts for lithium-oxygen batteries. The first step in the synthesis is the direct growth of TCNQ nanoarrays on commercial carbon cloth at room temperature, utilizing a chemical solution deposition approach. Subsequently, low-temperature phosphidation reactions are carried out, as detailed in the experimental section and Figure 1. A single Cu_3P phase could be easily created through a simple synthesis method using MOFs.

This study focuses on the characterization and comparative analysis of the catalytic activity of nanoarrays synthesized at a fast growth rate versus the congeners synthesized at a slow growth rate. As an integrated three-dimensional (3D) carbon cloth cathode for highly efficient oxygen reduction in LOBs, SG-Cu_3P NAs/CC exhibits sustained activity over a considerable number of cycles (115 cycles) and affords a low overpotential of 1.18 V at the first cycle. In the first deep discharge cycle, a high capacity of 9.68 mA h cm^{-2} was recorded at a current density of 0.1 mA cm^{-2}. The catalytic active area is assessed using electric double-layer capacitor (EDLC) and cyclic voltammetry (CV) methods. The effectiveness of the catalyst in oxygen reactions is attributed to both the structural stability and substantial catalytic active area. The in situ Raman spectroscopic analyses during deep discharge/charge cycles further corroborate the effectiveness of SG-Cu_3P NAs/CC for promoting the ORR and OER while suppressing undesired side reactions.

2. Results and Discussion

2.1. Characterization of Copper Phosphide Electrocatalysts. The process for fabricating the self-supported Cu_3P nanoarrays on the carbon cloth (Cu_3P NAs/CC) is illustrated in Figure 1. A two-step sequential phosphidation process was used to achieve uniform growth of nanoarrays directly on the carbon cloth substrate. First, Cu chloride solution was dried and heat-treated to form a copper seed layer on carbon cloth (Cu/CC), as shown in Figure S1. Thereafter, CuTCNQ nanoarrays (CuTCNQ/CC) were deposited on the surface of Cu/CC by the TCNQ-solution method. The configuration of CuTCNQ comprises distinctively stacked CuTCNQ units with specific distances between the CuTCNQ units, in which the quinoid rings of the CuTCNQ units engage in interplanar stacking along the *c*-axis [48]. Here, Cu atoms pass through the positions where the coordination changes. Consequently, the CuTCNQ units form nanoarrays and function as a structural framework with inherent pores, establishing an intriguing framework for applications in energy storage fields. The three-dimensional framework concurrently serves as a source of both N and C, facilitating the creation of active nitrogen-doped carbon. When CuTCNQ/CC was pyrolyzed-phosphated at 300°C for 2 h under Ar atmosphere, CuTCNQ/CC was transformed into Cu_3P NAs/CC.
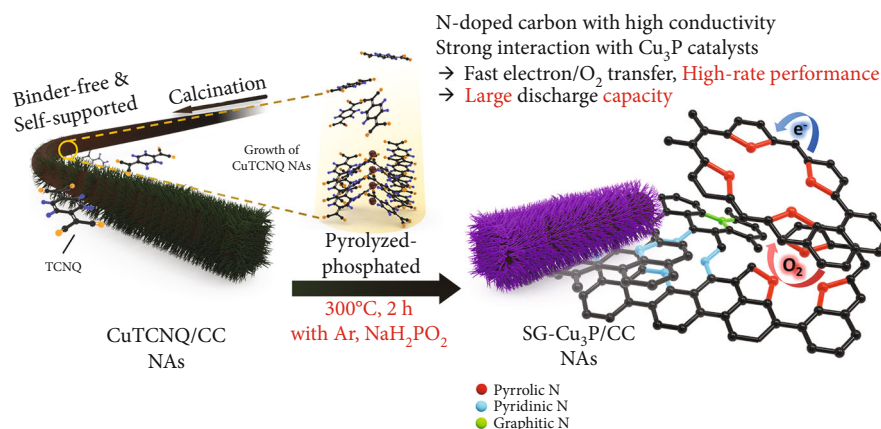
FIGURE 1: Schematic of the synthesis and mechanism of growth of Cu_3P nanoarrays from CuTCNQ nanowires.

The influence of the temperature ramping rate during phosphidation on the nanostructures was first investigated by scanning electron microscopy (SEM), as shown in Figures 2(a)–2(c). CuTCNQ, which consisted of uniform nanoarrays with diameters ranging from 432 nm to 649 nm, was formed on carbon cloth at room temperature by chemical solution deposition. After the phosphidation process at fast and slow heating rates, the 1D nanoarray structure was still preserved (Figures 2(b) and 2(c)). The fast heating rate during the phosphidation process led to a significant morphological transformation of the sharp CuTCNQ nanoarrays to a notably bent configuration (Figure 2(b)). In contrast, when the phosphidation temperature was raised gradually, the straight configuration of the nanoarrays was stably preserved (Figure 2(c)).

Figures 2(d) and 2(e) present the TEM images of a single FG-Cu_3P NAs and SG-Cu_3P NAs unit, respectively, showing that the pointed tip of TCNQ became more blunt after phosphidation (Figure S2). In FG-Cu_3P NAs/CC, large crystal grains were connected to form an array, whereas in SG-Cu_3P NAs/CC, small particles were evenly spread across an array inside a uniform carbon nanoarray. The particle size distribution and average particle diameter ($d_{average}$) were evaluated from the TEM images (Figure S3), with SG-Cu_3P NAs comprising smaller particles ($d_{average} = 4.58 \pm 1.28$ nm) than FG-Cu_3P NAs ($d_{average} = 6.90 \pm 2.57$ nm). This difference is attributed to the slower growth rate during the synthesis of SG-Cu_3P NAs/CC as compared to the faster rate for FG-Cu_3P NAs/CC. In the case of SG-Cu_3P NAs/CC, the nanoparticles were clearly more evenly dispersed along the nanoarrays, attributed in part to the intentional control of the phase formation time, which enabled sufficient nucleation and growth. Synthesis of the FG-Cu_3P NAs/CC at a fast heating rate most likely results in the formation of larger crystalline and various undesired phosphide species, which tend to easily agglomerate on the surface [49, 50]. The high-resolution transmission electron microscopy (HR-TEM) images show distinct lattice fringes with an interplanar distance of 2.22 Å in SG-Cu_3P NAs/CC; this distance was indexed to the (121) planes of Cu_3P (Figure S4). However, for FG-Cu_3P NAs/CC, another interplanar distance of 2.81 Å was observed, consistent with the ($\bar{1}$12) plane of CuP_2, as a secondary phase.

The nanoarray structures were further characterized using XRD. Figure 2(f) shows that all diffraction peaks are in accordance with the trigonal Cu_3P phase (PDF No. 72-1330). The diffraction peaks at 28.1°, 35.7°, 38.7°, 41.0°, 44.3°, 46.0°, and 46.8° were assigned to the (111), (112), (202), (121), (300), (113), and (122) planes, respectively. During the slow phosphidation process, the main peaks of CuTCNQ became significantly less intense, accompanied by transformation to the single Cu_3P phase SG-Cu_3P NAs/CC [43]. In FG-Cu_3P NAs/CC comprising nanoarrays with bent ends, a secondary CuP_2 phase, indicated by peaks at 22.5°, 30.9°, 33.5°, and 40.6°, was formed during the phosphidation reaction at a rapid temperature rise rate. These peaks are attributed to the (011), ($\bar{1}$12), (200), and (112) planes of monoclinic CuP_2 (PDF No. 18-0452).

X-ray photoelectron spectroscopy (XPS) analyses were conducted to examine the surface oxidation state and chemical composition. Figure S5 illustrates a representative XPS survey scan encompassing Cu 2p, O 1s, N 1s, C 1s, and P 2p peaks for CuTCNQ, FG-Cu_3P NAs/CC, and SG-Cu_3P NAs/CC. The broad peaks were assigned as satellite peaks and located at 941.7 and 943.9 eV for Cu $2p_{3/2}$ and 961.8 eV and 962.4 eV for Cu $2p_{3/2}$ (Figure 3(a) and Table S1). Peaks located at higher energy correspond to satellite peaks (943.9 and 962.4 eV) related to Cu^+, while those at lower energy are associated with Cu^{2+} satellite peaks (941.7 and 961.8 eV) [51]. The higher proportion of Cu^+ satellite peaks is attributed to Cu^+ ions in the Cu_3P single phase. Regarding the satellite peaks, SG-Cu_3P NAs/CC and FG-Cu_3P NAs/CC exhibit different tendency. SG-Cu_3P NAs/CC displays distinct and intense peaks, indicating strong adsorption of oxygen molecules and surface CuO formation mediated by Cu^+ and Cu^{2+} [48, 52, 53]. This suggests that SG-Cu_3P NAs/CC is associated with stronger surface adsorption of oxygen molecules. In contrast, FG-Cu_3P NAs/CC show indistinct satellite peaks with lower intensity, suggesting relatively lower oxygen molecule adsorption capability.

However, the Cu 2p signal obtained after phosphidation was deconvoluted into four peaks including satellite peak. The new peaks at 936.0 and 955.5 eV were indexed to Cu^{2+} in the oxidized copper derived from surface oxidation in air [52]. The peaks at 934.5 and 954.1 eV were assigned to
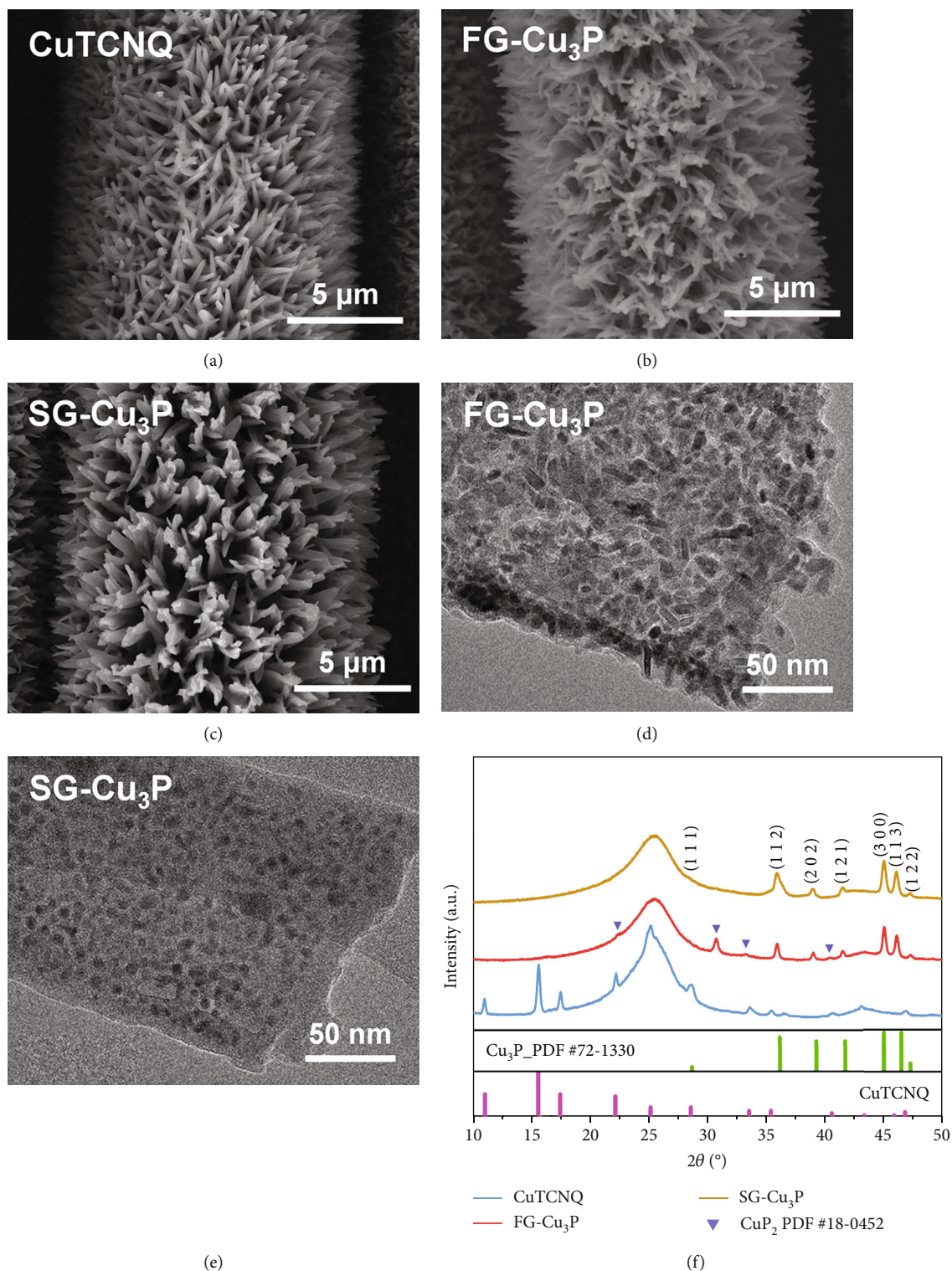
FIGURE 2: Field-emission SEM images of (a) CuTCNQ, (b) FG-Cu$_3$P, and (c) SG-Cu$_3$P NAs/CC. TEM images of (d) FG-Cu$_3$P and (e) SG-Cu$_3$P NAs/CC. (f) XRD patterns of CuTCNQ, FG-Cu$_3$P, and SG-Cu$_3$P NAs/CC.

the Cu 2p$_{3/2}$ and Cu 2p$_{1/2}$ electronic states of Cu$^+$ [53]. The relatively high Cu$^+$ ratio of SG-Cu$_3$P NAs is attributed to Cu$^+$ in single-phase Cu$_3$P. Two peaks appeared at low binding energies of 932.6 and 952.5 eV, corresponding to the Cu 2p$_{3/2}$ and Cu 2p$_{1/2}$ energy levels, respectively, attributed to

Cu^0 or Cu–P bonds [54]. It was confirmed that FG-Cu$_3$P NAs indeed exhibits a significant presence of strong Cu^0 or Cu–P bonds, constituting approximately 55.0% of the bonding ratio (compared to about 45.4% for SG-Cu$_3$P NAs). This indicates that the inclusion of the CuP$_2$ secondary phase is
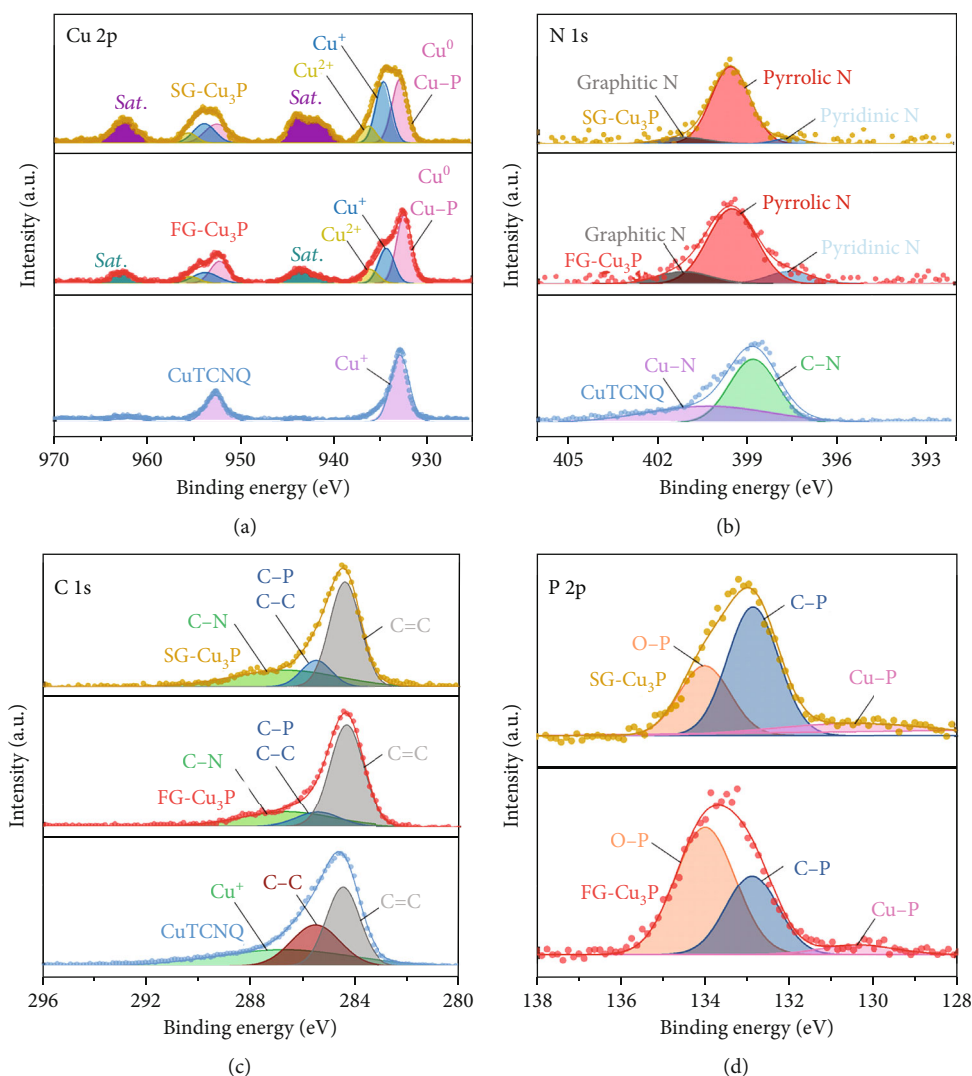
FIGURE 3: Magnified X-ray photoelectron spectroscopy (XPS) profiles of CuTCNQ, FG-Cu$_3$P, and SG-Cu$_3$P NAs/CC: (a) Cu 2p, (b) N 1s, (c) C 1s, and (d) P 2p.

associated with the strong Cu^0 or Cu–P bonds in the structure of FG-Cu$_3$P NAs, as revealed by XRD and TEM analysis, demonstrating the formation of a secondary surficial CuP$_2$ phase.

The N 1s spectra of CuTCNQ (Figure 3(b)) were deconvoluted into signals of Cu–N (398.7 eV) and C–N (400.2 eV), respectively (Table S2) [48]. The FG-Cu$_3$P and SG-Cu$_3$P NAs/CC units presented three peaks at 397.5, 399.5, and 401.1 eV, attributed to pyridinic, pyrrolic, and graphitic N, respectively [55, 56]. Table S3 summarizes the types and relative concentrations of nitrogen species in the samples. SG-Cu$_3$P NAs/CC possessed the highest relative concentrations of pyridine N and graphitic N, which are effective active sites that regulate the electronic structure of adjacent carbon atoms and increase the limiting current density, thereby enhancing the ORR activity [57]. The peaks at 284.4, 285.5, and 286.7 eV in the C 1s region of the spectrum correspond to C=C, C–P/C–C, and C–N, respectively (Figure 3(c)) [54]. These results reveal that N was introduced into the carbon nanoarray from the CuTCNQ. The incorporation of nitrogen

into a carbon matrix is well established to have a dual effect, enhancing the electrical conductivity while simultaneously inducing defect formation. In general, the incorporation of nitrogen into a carbon matrix offers advantages in terms of enhancing the electrical conductivity and promoting defect formation. Additionally, SG-Cu$_3$P NAs manifests a higher proportion of C–P bonding (13.8% for SG-Cu$_3$P NAs and 11.1% for FG-Cu$_3$P NAs, Table S4) [58]. This result substantiates the formation of strong electrical interactions between Cu$_3$P nanoparticles and the carbon matrix in SG-Cu$_3$P NAs. This synergistic effect between Cu$_3$P and N-doped carbon can increase both the active sites and stability of the catalyst, ensuring high-rate cyclability for LOBs.

The signal in the P 2p region of the spectrum was fitted by three peaks, attributed to P–Cu (130.5 eV), C–P (132.9 eV), and P–O (134.0 eV) (Figure 3(d)) [51, 59]. For SG-Cu$_3$P NAs/CC, the C–P area ratio (54.4%) was higher than that of FG-Cu$_3$P NAs/CC (33.0%) (Table S5). These results indicate a strong interaction between Cu$_3$P and the carbon matrix, consistent with the data from the C 1s

spectrum. The strong peak at higher binding energy (P–O bonding), assigned to oxidized phosphorus species, results from the surface oxidation of FG-Cu$_3$P NAs/CC. This partial superficial oxidation of FG-Cu$_3$P NAs/CC is a common phenomenon associated with the CuP$_2$ secondary phase. Overall, the strong C–P bonding within the carbon matrix can structurally stabilize SG-Cu$_3$P NAs/CC and contribute to excellent catalytic activity via rapid electron transfer through the nanoarrays.

2.2. Electrocatalytic Performance of Copper Phosphide Catalysts.

The electrode kinetics and resistance of the copper phosphides were meticulously investigated using electrical impedance spectroscopy (EIS), offering valuable insights into the interfacial processes within the system (Figure 4(a)). EIS tests were systematically conducted using electrodes within a full-cell system configuration, and the data were fitted based on the equivalent circuit model presented in Figure 4(a). In the Nyquist plot, the intersection of the impedance curve with the Z' real axis in the high-frequency region indicates the ohmic resistance (R_b), while the diameter of the semicircle reflects the charge transfer resistance (R_{ct}). A low R_b value of 3.45 Ω for the SG-Cu$_3$P NAs/CC electrode compared to that of the CuTCNQ/CC (5.51 Ω) and FG-Cu$_3$P NAs/CC (5.12 Ω) electrodes is presented in Table S6.

This difference indicates that the SG-Cu$_3$P NAs/CC electrode exhibits lower contact resistance in the LOB system. Moreover, the R_{ct} of the SG-Cu$_3$P NAs/CC electrode was significantly smaller (~63.3 Ω) than that of the CuTCNQ/CC (143 Ω) and FG-Cu$_3$P NAs/CC (108 Ω) electrodes, suggesting that the reaction kinetics at the electrode were effectively enhanced due to facilitated electron transfer along the nanoarrays of SG-Cu$_3$P. In addition, the intrinsic lithium-ion diffusion coefficient (D_{Li}) is calculated as shown in Figure S6 [60]. The Warburg factor (σ) is determined from the slope of the relationship between real resistance (Z') and inverse square root of angular speed ($\omega^{-1/2}$) at low-frequency region. D_{Li} of SG-Cu$_3$P NAs/CC and FG-Cu$_3$P NAs/CC were 1.40×10^{-15} and 4.30×10^{-16} cm^2 s^{-1}, respectively. These results suggest that well-dispersed Cu$_3$P particles closely connected to carbon nanoarrays can enable superior charge transport kinetics and facilitate effective charge transfer.

The electrocatalytic activity of the copper phosphides towards the ORR/OER was investigated using linear sweep voltammetry (LSV) by employing a full-cell system under identical conditions to those used for the EIS measurements. The results of the LSV analysis for the CuTCNQ, FG-Cu$_3$P, and SG-Cu$_3$P NAs/CC electrodes are presented in Figure 4(b). The SG-Cu$_3$P NAs/CC electrode exhibited a notably higher current density during the ORR process, compared with that of both the CuTCNQ and FG-Cu$_3$P NAs/CC electrodes. Furthermore, the SG-Cu$_3$P NAs/CC electrode demonstrated a higher onset potential of 2.78 V, surpassing that of the CuTCNQ/CC (2.67 V) and FG-Cu$_3$P NAs/CC (2.75 V) electrodes. These results indicate the superior ORR activity of SG-Cu$_3$P NAs/CC in efficiently catalyzing the formation of Li$_2$O$_2$ during the discharge process.

Subsequent to the assessment of the ORR activity, the OER activity of the copper phosphide electrodes was examined. The SG-Cu$_3$P NAs/CC electrode exhibited markedly better OER activity, characterized by a substantially higher current density than that of the CuTCNQ and FG-Cu$_3$P NAs/CC electrodes. The peak at 3.6–3.7 V corresponds to the delithiation process during oxidation; specifically, the transformation of Li$_2$O$_2$ to Li$_{2-x}$O$_2$ and nonstoichiometric Li$_{2-x}$O$_2$, possessing electronic conductivity akin to that of semiconductors or even semimetals, leads to the improved electrochemical performance of lithium-oxygen batteries. Upon charging at 4.25 V, Li$_{2-x}$O$_2$ undergoes further oxidation to lithium ions and oxygen. SG-Cu$_3$P NAs/CC, consisting of single-phase Cu$_3$P, afforded a higher oxidation current than FG-Cu$_3$P NAs/CC with the secondary CuP$_2$ phase, indicating accelerated decomposition kinetics and reduced electrochemical polarization in the former. The SG-Cu$_3$P NAs/CC featuring single-phase Cu$_3$P within carbon nanoarrays exhibit superior OER activity through the advantageous rapid electron transfer. In contrast, FG-Cu$_3$P NAs/CC is not advantageous for achieving improved OER activity as the large CuP$_2$ particles are concentrated on the surface.

From an alternative perspective, a high active surface area is not only beneficial but is also a prerequisite for the efficient performance of electrocatalysts. To evaluate the electrochemical active surface area (ECSA) of the CuTCNQ, FG-Cu$_3$P, and SG-Cu$_3$P NAs/CC electrodes, EDLC measurements were conducted in 1 M lithium bis(trifluoromethylsulfonyl)imide (LiTFSI) in N,N-dimethylacetamide (DMAc) electrolyte. Unlike traditional EDLC measurements in aqueous systems, a full-cell system with an organic electrolyte was utilized and O$_2$ pressure was applied to enable a more accurate analysis of the active sites for lithium and oxygen ions. CV were recorded at various scan rates (10, 20, 50, 100, 150, and 200 mV s^{-1}); the resulting profiles are illustrated in Figures 4(c) and 4(d) and Figure S7. The current, which represents half the difference between the forward and reverse currents at the middle of the potential window, was plotted against the scan rate.

The selected potentials (2.9–3.1 V, purple area in Figure 4(b)) lie in the non-Faradaic region of each catalyst and were compared with those of the control catalysts. The double-layer capacitance (C_{dl}) was estimated by examining the linear plots (Figure 4(e)). The ECSA values for the CuTCNQ, FG-Cu$_3$P, and SG-Cu$_3$P NAs/CC electrodes were determined to be 0.48, 0.55, and 0.70 mF, respectively. The higher capacitance observed for the SG-Cu$_3$P NAs/CC electrode suggests that it possesses the highest number of active sites and consequently exhibits the highest surface catalytic activity among the catalysts. These results demonstrate the enhanced catalytic activity of SG-Cu$_3$P NAs/CC, attributed to the improved anion exchange at the electrolyte-electrode interface due to the increased number of catalytically active sites, consistent with the improved onset potential values [61].

2.3. Rate Capability and Cycle Performance of Rechargeable LOBs.

A binder-free cathode was prepared by direct synthesis of SG-Cu$_3$P NAs on carbon cloth (with a mass ratio of 66 : 1) and was used as the oxygen cathode in a Swagelok-
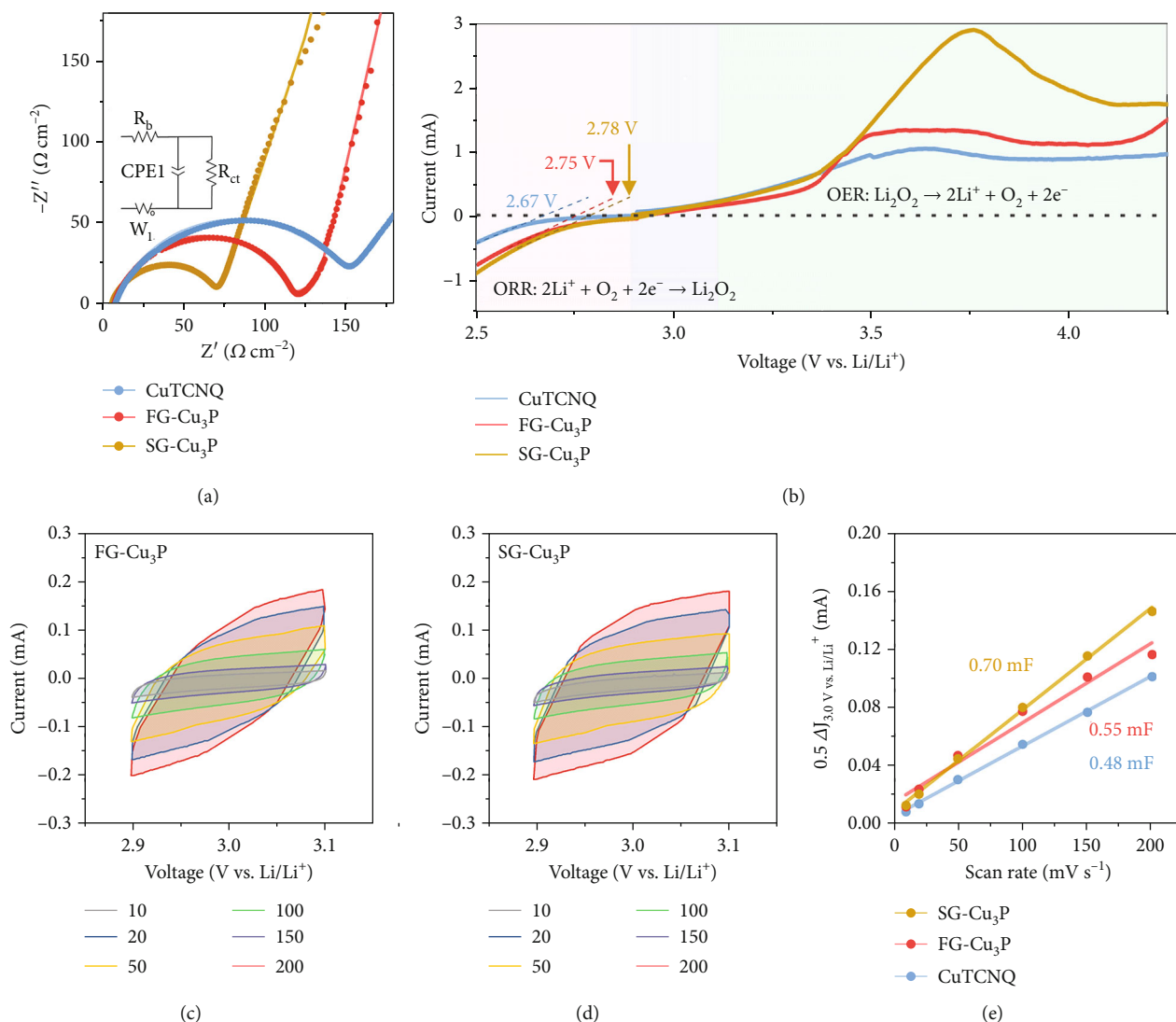
FIGURE 4: (a) Resistive-capacitive (RC) equivalent circuit model and Nyquist plots of CuTCNQ, FG-Cu$_3$P, and SG-Cu$_3$P NAs/CC electrodes for evaluating charge transfer. (b) ORR and OER linear sweep voltammetry of CuTCNQ, FG-Cu$_3$P, and SG-Cu$_3$P NAs/CC electrodes at a scan rate of 10 mA s^{-1}. Double-layer capacitance measurements for determining electrochemically active surface area of (c) FG-Cu$_3$P and (d) SG-Cu$_3$P NAs/CC electrodes. (e) Half of the difference in current density as a function of the scan rate.

type Li-O$_2$ cell. Figure 5(a) shows the 1st galvanostatic discharge-charge curves of the CuTCNQ, FG-Cu$_3$P, and SG-Cu$_3$P NAs/CC electrodes at a current density of 0.1 mA cm^{-2} within the voltage window of 2.0–5.0 V. The SG-Cu$_3$P NAs/CC electrodes exhibit the highest capacity of 9.69 mA h cm^{-2}, compared to the other electrodes (1.62 mA h cm^{-2} for CuTCNQ and 2.86 mA h cm^{-2} for FG-Cu$_3$P NAs/CC electrodes). The SG-Cu$_3$P NAs/CC electrode also afforded the lowest overpotential (1.13 V) at a capacity of 2 mA h cm^{-2}. It is widely discussed that P-doped carbon materials adopt sp^3 hybridization, leading to longer C–P bonds compared to C–C bonds due to the larger atomic radius of P, thereby inducing structural distortion in the carbon matrix. P doping effects charge redistribution within the material, with P serving as active sites for reactions [62]. The high proportion of C–P bonding supports the increased selectivity towards oxygen species, implying their role as active sites for the ORR [63]. The uniformly distributed

active sites along the nanoarrays induce homogeneous adsorption of oxygen species, contributing to the formation of smooth and large Li$_2$O$_2$ growth along the nanoarray direction during discharge [64]. These effects are deeply related to the capacity of the LOBs.

Galvanostatic discharge-charge cycling of each electrode was conducted at a current rate of 0.1 mA cm^{-2} and fixed capacity limit of 0.5 mA h cm^{-2} (Figures 5(b)–5(e)). The overpotential at the end voltage and cycle performance of the electrodes are compared in Figure 5(b). The CuTCNQ electrode, which exhibits high overpotentials, presented a rapid capacity drop within 40 cycles (Figure 5(c)). The SG-Cu$_3$P NAs/CC electrode indeed displays significant catalytic activity during the cycling. In contrast to the lower stability of CuTCNQ, SG-Cu$_3$P NAs/CC exhibit stability of 115 cycles. Furthermore, compared to FG-Cu$_3$P NAs/CC, SG-Cu$_3$P NAs/CC electrode shows a relatively lower overpotential (0.06 V) at 75 cycles (Figures 5(d) and 5(e)). The
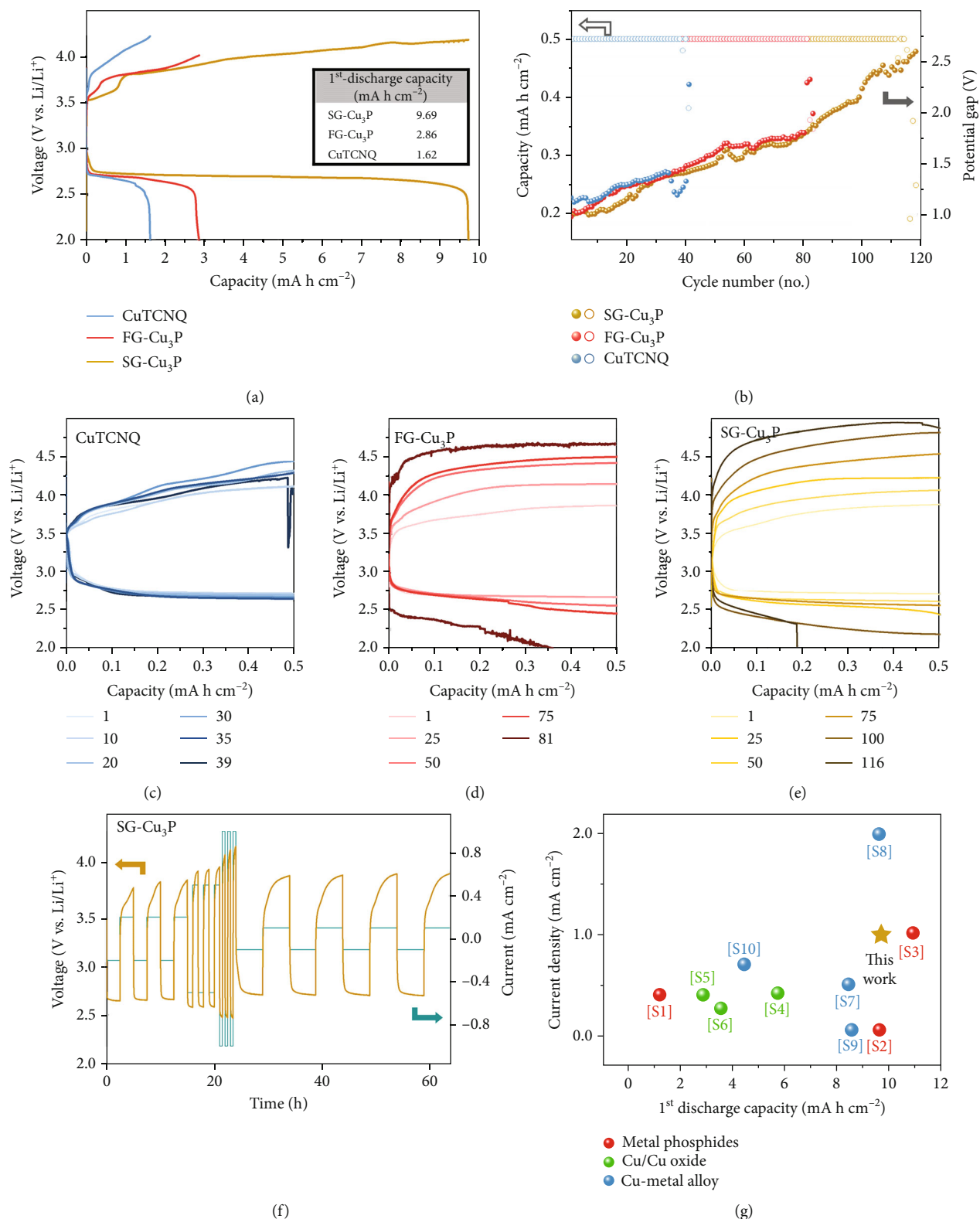
FIGURE 5: (a) First galvanostatic discharge-charge curves of CuTCNQ, FG-Cu$_3$P, and SG-Cu$_3$P NAs/CC electrodes at a current rate of 0.1 mA cm^{-2}. (b) Cycling performance and overpotential at end capacity for CuTCNQ, FG-Cu$_3$P, and SG-Cu$_3$P NAs/CC electrodes. Galvanostatic discharge-charge curves during cycling of (c) CuTCNQ, (d) FG-Cu$_3$P, and (e) SG-Cu$_3$P NAs/CC electrodes at a current rate of 0.1 mA cm^{-2} and fixed capacity limit of 0.5 mA h cm^{-2}. (f) Rate capability of SG-Cu$_3$P NAs/CC electrode at various current rates. (g) Comparison of the current density and cycle performance with those of previously reported metal phosphide electrocatalysts.

relatively lower termination voltage of the SG-Cu_3P NAs/CC electrode compared to that of the FG-Cu_3P NAs/CC electrode is plausibly due to the excellent Li_2O_2 oxidation activity of the SG-Cu_3P NAs/CC. The high-rate capability of the SG-Cu_3P NAs/CC electrode at a current rate of 0.5 mA cm^{-2} was also estimated, as shown in Figure S8. The overvoltage was stably maintained for ~30 cycles, and the end voltage difference was almost the same (2.05 V). The discharge-charge overpotential profile of the SG-Cu_3P NAs/CC electrode remained consistent during cycling, indicating relatively long cycle retention. Therefore, the lower overpotential of the SG-Cu_3P NAs/CC electrode compared to that of the other electrodes is due to its reversible catalytic activity, leading to improved round-trip efficiency and cycle stability during the discharge-charge process.

The rate capability of oxygen electrodes is a crucial aspect to consider when evaluating the practical applicability of aprotic LOBs. In assessing the rate performance of the SG-Cu_3P NAs/CC electrodes in LOBs, the electrodes were analyzed at different current densities and the overpotential at the end of each cycle was calculated (Figure 5(f)). Current densities of 0.1, 0.2, 0.5, and 1 mA cm^{-2} were applied, and the rate capability of the SG-Cu_3P NAs/CC electrode was assessed over three cycles at each rate. As the current density increased, the overpotential between the discharge and charge plateaus (representing the end of the discharge capacity) increased from 1.11 V (0.2 mA cm^{-2}) to 1.68 V (1 mA cm^{-2}). However, the difference in the overpotential at a given current density was not substantial. Notably, following cycling at a current density of 1 mA cm^{-2} (after 24 h), the cycling remained stable without any significant overvoltage changes and an overpotential of 2.43 V was sustained for more than 1000 h at a current density of 0.1 mA cm^{-2} (Figure S9). The SG-Cu_3P NAs/CC electrode exhibited exceptional rate capability over a broad range of current densities.

A comparative analysis of the current density and cycle performance of the developed electrode, in relation to those of previously reported metal phosphide electrocatalysts, is presented in Figure 5(g), and detailed performance metrics are provided in Table S7. The electrocatalytic performance of the SG-Cu_3P NAs/CC electrode with self-supported nanoarrays was superior, as indicated by the cyclability, compared to that of the other metal phosphide electrocatalysts under the specific operational conditions employed in the present tests (capacity limit of 0.5 mA h cm^{-2} and current density of 0.1 mA h cm^{-2}). In summary, the combination of low polarization from the uniformly dispersed Cu_3P nanoparticles in the N-doped carbon matrix, diverse array of active sites, excellent ionic conductivity, and suitable nanoarray structure of SG-Cu_3P results in low overpotential characteristics, even at high current rates, during continuous cycling.

The in situ electrochemical Raman spectroscopy was used to complement the valuable electrochemical data, providing direct spectroscopic evidence of the species present on the electrode surface and providing insights into the O_2 oxidation/reduction mechanism (Figure 6). To elucidate the impact of the superior catalytic activity of SG-Cu_3P NAs/CC on the aprotic oxygen reaction, the 1st discharge/charge curves were acquired at various time intervals, as indicated by the orange and blue markers. The discharge-charge profiles within the voltage range of 2.0–5.0 V at a current density of 0.25 mA cm^{-2} are presented in Figure 6(a). The SG-Cu_3P NAs/CC electrode exhibited a notable discharge capacity of 3.15 mA h cm^{-2} and a low overpotential of 1.51 V at the end capacity.

The Raman spectra acquired in the corresponding discharge state (marked with an orange marker (Figure 6(b))) showed new peaks, which were assigned to Li_2O_2 (788 cm^{-1}) and LiO_2 (1139 cm^{-1}) products [65, 66]. During the initial discharge stage (after 4 h), Li_2O_2 and LiO_2 peaks were evident. The LiO_2 detected on the electrode surface is known as an intermediate species in the formation of Li_2O_2, supporting the surface mechanism. In the 1 M LiTFSI in DMAc electrolyte, LiO_2 is generated on the surface of the 1D nanoarray catalyst and subsequently reacts with lithium ions, forming Li_2O_2 products. This formation of LiO_2 suggests a uniform distribution of active sites across the catalyst surface. Reversible and efficient performance of LOBs can be achieved by reducing the oxidation/reduction overpotentials through the uniform generation of LiO_2 and Li_2O_2 on the electrode surface.

As the discharge process continued, the discharge voltage decreased, and concurrently, the Li_2O_2 peak gained intensity. This indicates that Li_2O_2 is continuously formed during the discharge process (yellow ball, after 8 h discharge). However, during the third discharge stage (after 12 h discharge), the intensity of the peak corresponding to surficial LiO_2 became less intense, suggesting that the conversion of LiO_2 to Li_2O_2 is significantly accelerated at lower potentials (below 2.5 V) [67]. During subsequent discharge, the reaction continued until only the final Li_2O_2 discharge product was formed, accompanied by an increase in the overpotential.

During the initial charging process (blue ball, after 4 h charge), the Raman spectrum displayed peaks corresponding to both Li_2O_2 and LiO_2 products. The decrease in the intensity of the Li_2O_2 peak and the presence of the LiO_2 peak after discharge indicate the oxidation of Li_2O_2 and the simultaneous formation of LiO_2, which drives the OER. In the next charging stage (after 8 h charge), the intensity of the Li_2O_2 peak continued to diminish and the LiO_2 peak was barely observable, illustrating that the Li_2O_2 products are continually decomposed through the intermediate LiO_2. In the final stage (after 12 h charge), neither Li_2O_2 nor LiO_2 peaks were detected, indicating the effective catalytic effect of the SG-Cu_3P NAs/CC for oxidation. Moreover, the absence of side products such as Li_2CO_3 (1090 cm^{-1}) at higher charging voltages demonstrates the electrochemical stability and reversibility of the oxygen reaction [68]. We analyzed information of the morphological alterations of Cu_3P nanoarrays subsequent to actual full-charge and full-discharge processes conducted within a highly oxidized environment (2 bar of O_2 gas), using lithium-oxygen batteries (Figure S10A). The 1st discharge capacity of SG-Cu_3P NAs/CC presents 3.15 mA h cm^{-2}, while FG-Cu_3P NAs/CC shows 1.06 mA h cm^{-2} at a current rate of 0.25 mA cm^{-2}. This investigation is related to ascertaining the reversibility of SG-Cu_3P NAs. Preserving the structural configuration throughout cycling is a critical factor influencing catalyst activity. Detailed examination via FESEM reveals that
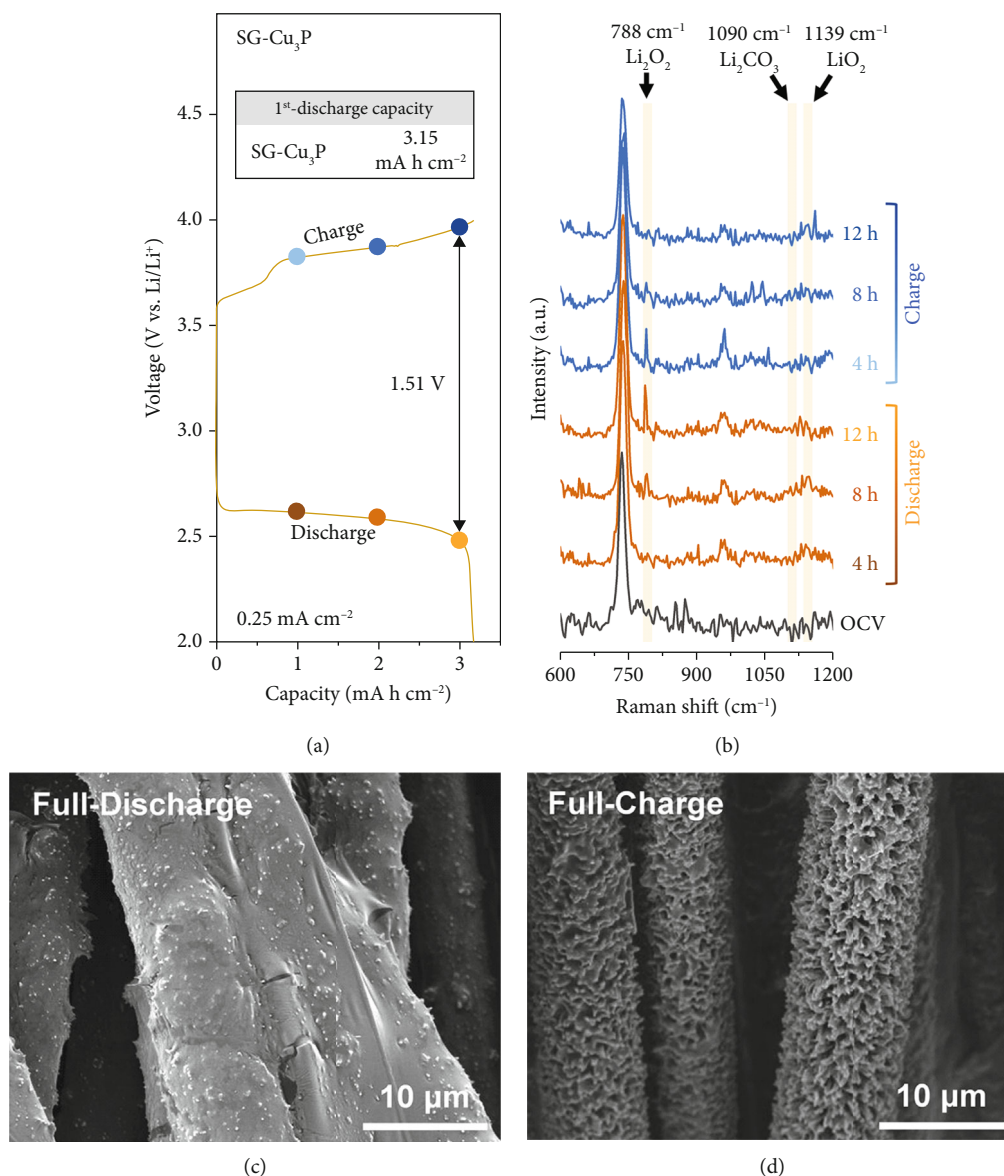
(a)

(b)

(c)

(d)

Figure 6: (a) First galvanostatic discharge-charge curves of SG-Cu$_3$P NAs/CC electrode at a current rate of 0.25 mA cm^{-2}. (b) In situ Raman spectra of SG-Cu$_3$P NAs/CC electrode from discharge to charge, recorded at 4 h intervals, corresponding to (a). SEM images of SG-Cu$_3$P NAs/CC electrode after (c) discharge and (d) charge processes.

following the discharge process, the SG-Cu$_3$P NAs/CC electrode becomes uniformly coated with Li$_2$O$_2$ products across its material surface (Figure 6(c)). In the contrast, it is observed that the FG-Cu$_3$P NAs/CC electrode exhibits uneven deposition of Li$_2$O$_2$ products upon the electrode material (Figure S10B). Subsequent to the charging process, the Li$_2$O$_2$ product undergoes complete decomposition, and the surface of SG-Cu$_3$P NAs/CC undergoes an effective recovery (Figure 6(d)). This behavior stems from the SG-Cu$_3$P NAs/CC facilitating the uniform formation and decomposition of Li$_2$O$_2$, thereby providing an increased number of active sites conducive to enhancing the ORR and OER activities. The enhanced concentration of surface-active sites promotes the adsorption of oxygen in the form of LiO$_2$ intermediates, enabling the formation of a uniform Li$_2$O$_2$ shell along the nanoarrays, as confirmed by the previous in

situ Raman spectroscopy. Conversely, the FG-Cu$_3$P NAs/CC electrode retains residual particles, which substantially impede battery performance by obstructing reaction sites and gas diffusion pores (Figure S10C). Therefore, it is demonstrated that subsequent to the charging process, SG-Cu$_3$P NAs/CC preserves its structural stability and reversibility for oxygen reactions, in contrast to FG-Cu$_3$P NAs/CC, which undergoes formation of uneven discharge products and structural deformation attributable to inherent instability.

By combined analysis of the Raman spectra with other experimental findings, it was confirmed that the Cu$_3$P NAs/CC electrode shows good reversibility at a high rate. The Cu$_3$P NAs/CC with numerous unsaturated active sites for the adsorption of oxygen-related species (LiO$_2$) follows a surface mechanism during cycling. During the discharge process, a uniform Li$_2$O$_2$ shell was formed along the Cu$_3$P

NAs with numerous active sites, followed by complete decomposition without residues during the charge process. Consequently, Cu_3P NAs/CC can be used directly as a cathode without binders, preventing the accumulation of parasitic side products, reducing the overpotential of the discharge and charge processes, and improving the rate capability at high current rates.

3. Experimental Section

3.1. Preparation of CuTCNQ/CC. CuTCNQ/CC was prepared by a modified literature method [32]. A Cu seed layer on carbon cloth was prepared by reduction heat treatment. $CuCl_2$ (0.3465 g, Sigma-Aldrich, 97%) was dissolved in ethyl alcohol (5 mL, Samchun, 99.9%). As-prepared $CuCl_2$ in ethanol solution (50 μL) was directly dropped onto carbon cloth (CeTech, diameter = 1 cm) and then dried under an incandescent light. The carbon cloths with the $CuCl_2$ seed layer were calcined under a reducing atmosphere (H_2/Ar20/80 sccm) at 400°C and held for 30 minutes (heating rate = 40°C min^{-1}).

Before the next precipitation step, acetonitrile solvent (Samchun, 99%) was prepared by purging with N_2 for 30 minutes, after which TCNQ (0.123 g, Sigma-Aldrich, 98%) was dissolved in the N_2-purged acetonitrile solvent (60 mL). Thereafter, Cu/CC was immersed in as-prepared TCNQ solution (5 mL) for 80 minutes. The solution and the carbon cloth surface changed color to green, indicating the formation of CuTCNQ/CC. The CuTCNQ/CC was washed with distilled water three times to remove residual TCNQ and dried in a vacuum.

3.2. Preparation of FG-Cu$_3$P and SG-Cu$_3$P NAs/CC. For phosphidation, six pieces of CuTCNQ/CC and NaH_2PO_2 (0.3 g, Sigma-Aldrich, 99%) were placed at the center and in the upstream zone of a quartz tube, respectively, and heat-treated at 300°C for 2 hours under flowing Ar gas (100 sccm). The heating rate for FG-Cu_3P/CC was set to 30°C min^{-1}, whereas that for SG-Cu_3P/CC was set to 1°C min^{-1}.

3.3. Characterization of Materials. The sample morphologies were assessed by using a dual-beam focused ion beam (FIB; Helios 600i FIB/SEM, FEI) instrument. Detailed lattice and structural information were obtained via TEM (JEOL, JEM-F200, Japan). The phase composition of the sample was determined using XRD (Rigaku Miniflex 600) at 40 kV and 15 mA. The surface chemical composition of the samples was analyzed using XPS (ULVAC-PHI, X-TOOL, Japan). The Raman spectra were recorded with a real-time confocal Raman microscope (HEDA, WEVE, Republic of Korea) under excitation at 532 nm using a diode. The slit width and grating were adjusted to 120 μm and 1200 g mm^{-1}, respectively. Each Raman spectrum was acquired over 300 s, with two acquisitions.

3.4. Electrochemical Measurement. The charge resistance of the catalysts was determined using EIS at room temperature using Swagelok-type cells. The anode consisted of lithium foil, and the cathode was composed of self-supported SG-Cu_3P NAs/CC. The electrolyte comprised 1 м LiTFSI (Alfa

Aesar, ≥98%) in DMAc (Alfa Aesar, anhydrous, ≥99.8%). No binders were used in the cell fabrication process. The loading mass of the oxygen electrode was adjusted to fall within the range of 0.13–0.26 mg cm^{-2}. The same carbon cloth used in the synthesis of CuTCNQ/CC served as the gas diffusion layer. The cell was assembled in an argon-filled glove box. EIS data were acquired in the impedance frequency range of 100 MHz to 0.1 Hz with an AC voltage amplitude of 10 mV. EIS analyses were performed using an electrochemical workstation (Ivium-n-Stat, Ivium Tech., Netherlands). LSV was used to evaluate the ORR/OER activities of the samples. For LSV analysis, the ORR/OER measurement was performed in the voltage ranges of 3.0–2.0 V and 3.0–4.6 V at a scan rate of 10 mV s^{-1}, respectively. LSV experiments were also performed using Swagelok-type cells under the same conditions. The EDLC was also evaluated using Swagelok-type cells. The potential range for EDLC was set to 2.9–3.1 V vs. Li/Li$^+$, and the scan rate was varied (10–200 mV s^{-1}). The Li-O_2 battery was assembled using the same procedure as described for the EIS measurements. Li-O_2 cell measurements were conducted within the voltage range of 2.0–5.0 V (vs. Li/Li$^+$). LSV, EDLC, and galvanostatic discharge-charge profiles were recorded using an automatic battery cycler (WBCS 3000, WonaTech) after an initial open circuit potential hold of 6 h.

The electrode employed in the Raman spectrum analysis was prepared using the same process used for the Swagelok-type cells. A uniform 65 μL drop of the electrolyte was applied to the top of the electrode, which was positioned on the GF separator. The lithium foil was subsequently assembled on top of the separator. Notably, a small hole was introduced in both the separator and lithium foil to position the electrode at the bottom structure of the cell, allowing for the easy passage of light and Raman signals. This cell assembly was carried out in an argon-filled glove box. Prior to the in situ Raman test, oxygen (1.5 bar) was introduced into the Raman cell. The equipment utilized for LSV was used to record the current and potential data during this analysis.

4. Conclusions

In conclusion, the study presents a novel approach to fabricating copper phosphide nanoarrays on carbon cloth (Cu_3P NAs/CC) through a two-step phosphidation process. The resulting self-supported nanoarrays demonstrated exceptional structural stability and electrocatalytic performance for lithium-oxygen batteries (LOBs). The influence of the phosphidation temperature ramping rate on the nanostructures was explored, revealing that a slow rate preserved the straight configuration of the nanoarrays compared to a fast rate, which led to morphological transformation. The slow phosphidation process resulted in a single-phase Cu_3P nanoarray structure (SG-Cu_3P NAs/CC), while a fast rate introduced a secondary CuP_2 phase (FG-Cu_3P NAs/CC). The SG-Cu_3P NAs/CC electrode exhibited superior electrocatalytic activity for oxygen reactions, attributed to its strong C-P bonding, diverse array of active sites, and efficient charge transport kinetics. SG-Cu_3P NAs/CC possesses more

electrochemically active sites, equivalent to 0.70 mF in the ECSA analysis, providing more active sites for catalytic reactions. The electrode demonstrated excellent rate capability $(0.1-1\,mA\,cm^{-2})$ and cycle performance (115 cycles) in rechargeable LOBs, outperforming other reported metal phosphide electrocatalysts. The in situ electrochemical Raman spectroscopy revealed that the LiO_2 intermediate was formed and eventually decomposed at the end of charging, following the surface mechanism. Formation of a uniform Li_2O_2 shell and its effective decomposition demonstrates the superior reversibility of the electrode, making it a promising candidate for high-performance LOBs. This study not only contributes to the understanding of nanostructured copper phosphide catalysts but also holds promise for advancing the development of high-performance lithium-oxygen battery systems.

Data Availability

Data is available on request.

Conflicts of Interest

The authors declare that there is no conflict of interest regarding the publication of this article.

Authors' Contributions

Chan Ho Kim and Myeong-Chang Sung contributed equally to this work.

Acknowledgments

Supplementary Materials

Additional supporting information may be found in the online version of the article at the publisher's website. Figure S1: SEM images of (A, B) pristine carbon cloth and (C, D) Cu seed on carbon cloth. Figure S2: TEM image of CuTCNQ nanoarray. Figure S3: particle size distribution of (A) FG-Cu_3P and (B) SG-Cu_3P NAs/CC. Figure S4: HR-TEM images of (A) FG-Cu_3P and (B) SG-Cu_3P NAs/CC. Figure S5: X-ray photoelectron spectroscopy (XPS) survey scan of CuTCNQ and FG-Cu_3P and SG-Cu_3P NAs/CC. Figure S6: relationship between real resistance (Z') and inverse square root of angular speed (at $\omega^{-1/2}$) low-frequency region. Figure S7: double-layer capacitance measurements for determining electrochemically active surface area of CuTCNQ electrode. Figure S8: (A) galvanostatic discharge-charge curves during cycling of SG-Cu_3P NAs/CC electrode at a current rate of $0.5\,mA\,cm^{-2}$ and fixed capacity limit of $0.5\,mA\,h\,cm^{-2}$. (B)

Cycle performance of SG-Cu_3P NAs/CC electrode corresponding to Figure S7A. Figure S9: rate capability of SG-Cu_3P NAs/CC electrode at various current rates. Figure S10: (A) first galvanostatic discharge-charge curves of SG-Cu_3P NAs/CC and FG-Cu_3P NAs/CC electrode at a current rate of $0.25\,mA\,cm^{-2}$. SEM images of FG-Cu_3P NAs/CC electrode after (B) discharge and (C) charge processes. Table S1: binding energies (eV) and area percentages (%) of elemental Cu from the XPS profiles of FG-Cu_3P and SG-Cu_3P NAs/CC. Table S2: binding energies (eV) and area percentages (%) of elemental Cu, N, and C from the XPS profiles of CuTCNQ/CC. Table S3: binding energies (eV) and area percentages (%) of elemental N from the XPS profiles of FG-Cu_3P and SG-Cu_3P NAs/CC. Table S4: binding energies (eV) and area percentages (%) of elemental C from the XPS profiles of FG-Cu_3P and SG-Cu_3P NAs/CC. Table S5: binding energies (eV) and area percentages (%) of elemental P from the XPS profiles of FG-Cu_3P and SG-Cu_3P NAs/CC. Table S6: corresponding EIS parameters of CuTCNQ, FG-Cu_3P, and SG-Cu_3P NAs/CC based on resistive-capacitive (RC) equivalent circuit model in Figure 4(a). Table S7: comparison of the electrocatalytic performance of the SG-Cu_3P NAs/CC electrode with those of metal phosphide electrocatalysts for Li-O_2 batteries. *(Supplementary Materials)*

References

[1] Y. S. Kim, G.-H. Lee, M.-C. Sung, and D.-W. Kim, "Orthorhombically distorted perovskite $SeZnO_3$ nanosheets as an electrocatalyst for lithium-oxygen batteries," *Chemical Engineering Journal*, vol. 406, article 126896, 2021.

[2] D. K. Kim, J. B. Park, C. Choi, and D.-W. Kim, "An oxygen-vacancy-boosted heterostructured catalyst with synergistically integrated dual transition-metal oxides for high-performance lithium-sulfur batteries," *Chemical Engineering Journal*, vol. 479, article 147820, 2024.

[3] X. Yan, L. Lin, Q. Chen et al., "Multifunctional roles of carbon-based hosts for Li-metal anodes: a review," *Carbon Energy*, vol. 3, no. 2, pp. 303–329, 2021.

[4] G. Yue, X. Luo, Z. Hu et al., "RuO_{2-x} decorated $CoSnO_3$ nanoboxes as a high performance cathode catalyst for Li–CO_2 batteries," *Chemical Communications*, vol. 56, no. 78, pp. 11693–11696, 2020.

[5] C. Lin, L. Ouyang, R. Hu et al., "Synthesis of amorphous SeP_2/C composite by plasma assisted ball milling for high-performance anode materials of lithium and sodium-ion batteries," *Progress in Natural Science: Materials International*, vol. 31, no. 4, pp. 567–574, 2021.

[6] L. Dong, W. Yang, W. Yang et al., "High-power and ultralong-life aqueous zinc-ion hybrid capacitors based on pseudocapacitive charge storage," *Nano-Micro Letters*, vol. 11, no. 1, p. 94, 2019.

[7] P. G. Bruce, S. A. Freunberger, L. J. Hardwick, and J.-M. Tarascon, "Li-O_2 and Li-S batteries with high energy storage," *Nature Materials*, vol. 11, no. 1, pp. 19–29, 2012.

[8] Z. Peng, S. A. Freunberger, Y. Chen, and P. G. Bruce, "A reversible and higher-rate Li-O_2 battery," *Science*, vol. 337, no. 6094, pp. 563–566, 2012.

[9] T. Liu, J. P. Vivek, E. W. Zhao, J. Lei, N. Garcia-Araez, and C. P. Grey, "Current challenges and routes forward for

nonaqueous lithium-air batteries," *Chemical Reviews*, vol. 120, no. 14, pp. 6558–6625, 2020.

[10] J.-W. Jung, S.-H. Cho, J. S. Nam, and I.-D. Kim, "Current and future cathode materials for non-aqueous Li-air (O₂) battery technology – a focused review," *Energy Storage Materials*, vol. 24, pp. 512–528, 2020.

[11] W.-J. Kwak, D. Rosy, C. Sharon et al., "Lithium-oxygen batteries and related systems: potential, status, and future," *Chemical Reviews*, vol. 120, no. 14, pp. 6626–6683, 2020.

[12] A. Zahoor, Z. K. Ghouri, S. Hashmi et al., "Electrocatalysts for lithium–air batteries: current status and challenges," *ACS Sustainable Chemistry & Engineering*, vol. 7, no. 17, pp. 14288–14320, 2019.

[13] G. Yue, Z. Hong, Y. Xia, T. Yang, and Y. Wu, "Bifunctional electrocatalysts materials for non-aqueous Li–air batteries," *Coatings*, vol. 12, no. 8, p. 1227, 2022.

[14] F. Wu, Y. Xing, X. Bi et al., "Systematic study on the discharge product of Pt-based lithium oxygen batteries," *Journal of Power Sources*, vol. 332, pp. 96–102, 2016.

[15] T. Qu, X. Lang, L. Li et al., "Ag modified NixAlyMnzO2 polynary metal oxides (Ag@NAM) synthesized by a facile precipitation method as bifunctional catalyst for high performance air electrode of lithium-oxygen batteries," *International Journal of Energy Research*, vol. 45, no. 10, pp. 15595–15603, 2021.

[16] L. Liu, T. Ma, W. Fang et al., "Facile fabrication of Ag nanocrystals encapsulated in nitrogen-doped fibrous carbon as an efficient catalyst for lithium oxygen batteries," *Energy & Environmental Materials*, vol. 4, no. 2, pp. 239–245, 2021.

[17] K.-H. Kwak, D. W. Kim, Y. Kang, and J. Suk, "Hierarchical Ru and RuO₂-foams as high performance electrocatalysts for rechargeable lithium-oxygen batteries," *Journal of Materials Chemistry A*, vol. 4, no. 42, pp. 16356–16367, 2016.

[18] L. Dai, Q. Sun, J. Guo et al., "Mesoporous Mn₂O₃ rods as a highly efficient catalyst for Li–O₂ battery," *Journal of Power Sources*, vol. 435, p. 226833, 2019.

[19] S. Shin, Y. Yoon, and M. W. Shin, "Co/Zn-based bimetallic MOF-derived hierarchical porous co/C composite as cathode material for high-performance lithium-air batteries," *International Journal of Energy Research*, vol. 46, no. 7, pp. 9900–9910, 2022.

[20] Y. S. Kim, G.-H. Lee, and D.-W. Kim, "TCNQ-derived N/S dual-doped carbon cube electrocatalysts with built-in CoS₂ nanoparticles for high-rate lithium-oxygen batteries," *Chemical Engineering Journal*, vol. 418, article 129367, 2021.

[21] R. Wang, B. Liu, S. You et al., "Three-dimensional Ni₃Se₄ flowers integrated with ultrathin carbon layer with strong electronic interactions for boosting oxygen reduction/evolution reactions," *Chemical Engineering Journal*, vol. 430, article 132720, 2022.

[22] P. Thakur, A. B. Puthirath, P. M. Ajayan, and T. N. Narayanan, "Iron carbide decorated carbon nanosphere-sheet hybrid based rechargeable high-capacity non-aqueous Li–O₂ batteries," *Carbon*, vol. 196, pp. 320–326, 2022.

[23] X. Li, G. Han, S. Lou et al., "Tailoring lithium-peroxide reaction kinetics with CuN₂C₂ single-atom moieties for lithium-oxygen batteries," *Nano Energy*, vol. 93, article 106810, 2022.

[24] J. Xiao, D. Mei, X. Li et al., "Hierarchically porous graphene as a lithium-air battery electrode," *Nano Letters*, vol. 11, no. 11, pp. 5071–5078, 2011.

[25] A. C. Lim, H. J. Kwon, H. C. Lee et al., "Mechanically reinforced-CNT cathode for Li-O₂ battery with enhanced spe-

[26] M. He, J. Jia, Q. Sun, and W. Zhang, "Hollow N-doped carbon sphere synthesized by MOF as superior oxygen electrocatalyst for Li-O₂ batteries," *International Journal of Energy Research*, vol. 45, no. 5, pp. 7120–7128, 2021.

[27] S. Wu, D. Wu, D. Zhang et al., "Boosting the activity and stability with dual-metal-N couplings for Li–O₂ battery," *Energy & Environmental Materials*, vol. 5, no. 3, pp. 918–927, 2022.

[28] M. Yuan, Z. Sun, H. Yang et al., "Self-catalyzed rechargeable lithium-air battery by in situ metal ion doping of discharge products: a combined theoretical and experimental study," *Energy & Environmental Materials*, vol. 6, no. 1, article E12258, 2023.

[29] J. Long, Z. Hou, C. Shu et al., "Free-standing three-dimensional CuCo₂S₄ nanosheet array with high catalytic activity as an efficient oxygen electrode for lithium-oxygen batteries," *ACS Applied Materials & Interfaces*, vol. 11, no. 4, pp. 3834–3842, 2019.

[30] Y. Liu, Y. Liu, H. Shi et al., "Cobalt-copper layered double hydroxide nanosheets as high performance bifunctional catalysts for rechargeable lithium-air batteries," *Journal of Alloys and Compounds*, vol. 688, pp. 380–387, 2016.

[31] S. Liu, M. Liu, Q. Xu, and G. Zeng, "Lithium ion conduction in covalent organic frameworks," *Chinese Journal of Structural Chemistry*, vol. 41, no. 11, pp. 2211003–2211017, 2022.

[32] H. Yoo, G.-H. Lee, M.-C. Sung, and D.-W. Kim, "Rational design of porous Ru-doped CuO nanoarray on carbon cloth: toward reversible catalyst layer for efficient Li-O₂ batteries," *International Journal of Energy Research*, vol. 46, no. 6, pp. 8120–8129, 2022.

[33] H. Wang, H. Chen, H. Wang et al., "Hierarchical porous FeCo₂O₄@Ni as a carbon- and binder-free cathode for lithium–oxygen batteries," *Journal of Alloys and Compounds*, vol. 780, pp. 107–115, 2019.

[34] T. Yang, Y. Xia, T. Mao et al., "Phosphorus vacancies and heterojunction interface as effective lithium-peroxide promoter for long-cycle life lithium–oxygen batteries," *Advanced Functional Materials*, vol. 32, no. 49, article 2209876, 2022.

[35] F. Zhang, M. Wei, J. Sui et al., "Cobalt phosphide microsphere as an efficient bifunctional oxygen catalyst for Li-air batteries," *Journal of Alloys and Compounds*, vol. 750, pp. 655–658, 2018.

[36] Z. Ran, C. Shu, Z. Hou et al., "Modulating electronic structure of honeycomb-like Ni₂P/Ni₁₂P₅ heterostructure with phosphorus vacancies for highly efficient lithium-oxygen batteries," *Chemical Engineering Journal*, vol. 413, article 127404, 2021.

[37] A. Kondori, Z. Jiang, M. Esmaeilirad et al., "Kinetically stable oxide overlayers on Mo₃P nanoparticles enabling lithium-air batteries with low overpotentials and long cycle life," *Advanced Materials*, vol. 32, no. 50, article e2004028, 2020.

[38] A. Kondori, M. Esmaeilirad, A. Baskin et al., "Identifying catalytic active sites of trimolybdenum phosphide (Mo₃P) for electrochemical hydrogen evolution," *Advanced Energy Materials*, vol. 9, no. 22, article 1900516, 2019.

[39] S. Lv, F. Gou, H. Wang et al., "Interface coupling of Ni₂P@Cu₃P catalyst to facilitate highly-efficient electrochemical reduction of nitrate to ammonia," *Applied Surface Science*, vol. 648, article 159082, 2024.

[40] S. Guo, Y. Sun, J. Wang, L. Peng, H. Li, and C. Li, "Bimetallic ZIF-derived cobalt nanoparticles anchored on N- and S-codoped porous carbon nanofibers as cathode catalyst

for Li-O$_2$ batteries," *Electrochimica Acta*, vol. 418, article 140279, 2022.

[41] G.-H. Lee, Y. S. Kim, M.-C. Sung, and D.-W. Kim, "Ultrafine CoP nanoparticles encapsulated in N/P dual-doped carbon cubes derived from 7,7,8,8-tetracyanoquinodimethane for lithium-ion batteries," *Applied Surface Science*, vol. 555, article 149716, 2021.

[42] G.-H. Lee, H. Yoo, and D.-W. Kim, "Porous carbon cubes decorated with cobalt nanoparticles for oxygen evolution catalysis in Zn-air batteries," *International Journal of Energy Research*, vol. 46, no. 5, pp. 6755–6765, 2022.

[43] R. Clérac, S. O'Kane, J. Cowen et al., "Glassy magnets composed of metals coordinated to 7,7,8,8-tetracyanoquinodimethane: M(TCNQ)$_2$ (M = Mn, Fe, Co, Ni)," *Chemistry of Materials*, vol. 15, no. 9, pp. 1840–1850, 2003.

[44] R. A. Heintz, H. Zhao, X. Ouyang, G. Grandinetti, J. Cowen, and K. R. Dunbar, "New insight into the nature of Cu(TCNQ): solution routes to two distinct polymorphs and their relationship to crystalline films that display bistable switching behavior," *Inorganic Chemistry*, vol. 38, no. 1, pp. 144–156, 1999.

[45] K. R. Yoon, J.-W. Jung, and I.-D. Kim, "Recent progress in 1D air electrode nanomaterials for enhancing the performance of nonaqueous lithium-oxygen batteries," *ChemNanoMat*, vol. 2, no. 7, pp. 616–634, 2016.

[46] M.-C. Sung, G.-H. Lee, and D.-W. Kim, "Efficient Li$_2$O$_2$ oxidation kinetics of perovskite-type lanthanum chromium-based oxide by promoter interface formation for lithium-oxygen batteries," *Energy Storage Materials*, vol. 60, article 102829, 2023.

[47] J. Rong, J. Xu, F. Qui et al., "Sea urchin-like MOF-derived formation of porous Cu$_3$P@C as an efficient and stable electrocatalyst for oxygen evolution and hydrogen evolution reactions," *Advanced Materials Interfaces*, vol. 6, no. 14, article 1900502, 2019.

[48] M. J. Capitan, J. Alvarez, and F. Yndurain, "Organometallic MTCNQ films: a comparative study of CuTCNQ versus AgTCNQ," *Physical Chemistry Chemical Physics*, vol. 20, no. 33, pp. 21705–21715, 2018.

[49] L. Zhang, H. Nakamura, C.-G. Lee, and H. Maeda, "An investigation of heating rate effects on particle size and concentration: instruction for scale-up," *RSC Advances*, vol. 2, no. 9, pp. 3708–3713, 2012.

[50] Y. Zhou, K. Hirao, Y. Yamauchi, and S. Kanzaki, "Effects of heating rate and particle size on pulse electric current sintering of alumina," *Scripta Materialia*, vol. 48, no. 12, pp. 1631–1636, 2003.

[51] J. A. Torres-Ochoa, D. Cabrera-German, O. Cortazar-Martinez, M. Bravo-Sanchez, G. Gomez-Sosa, and A. Herrera-Gomez, "Peak-fitting of Cu 2p photoemission spectra in Cu^0, Cu^{1+}, and Cu^{2+} oxides: a method for discriminating Cu^0 from Cu^{1+}," *Applied Surface Science*, vol. 622, article 156960, 2023.

[52] H. Wang, A.-J. Song, H. Chen, W.-M. Zhang, and Z.-H. Xue, "Charge-storage nickel substrate-boosted CuP$_2$ nanosheet for the electrochemical oxygen evolution reaction," *Inorganic Chemistry*, vol. 61, no. 32, pp. 12489–12493, 2022.

[53] S. Wei, K. Qi, Z. Jin et al., "One-step synthesis of a self-supported copper phosphide nanobush for overall water splitting," *ACS Omega*, vol. 1, no. 6, pp. 1367–1373, 2016.

[54] M. Kong, H. Song, and J. Zhou, "Metal-organophosphine framework-derived N,P-codoped carbon-confined Cu$_3$P Nanopaticles for superb Na-ion storage," *Advanced Energy Materials*, vol. 8, no. 27, article 1801489, 2018.

[55] B. P. Vinayan, N. I. Schwarzburger, and M. Fichtner, "Synthesis of a nitrogen rich (2D–1D) hybrid carbon nanomaterial using a MnO$_2$ nanorod template for high performance Li-ion battery applications," *Journal of Materials Chemistry A*, vol. 3, no. 13, pp. 6810–6818, 2015.

[56] S.-O. Kim and A. Manthiram, "The facile synthesis and enhanced sodium-storage performance of a chemically bonded CuP$_2$/C hybrid anode," *Chemical Communications*, vol. 52, no. 23, pp. 4337–4340, 2016.

[57] Z. Duan and G. Henkelman, "Identification of active sites of pure and nitrogen-doped carbon materials for oxygen reduction reaction using constant-potential calculations," *The Journal of Physical Chemistry C*, vol. 124, no. 22, pp. 12016–12023, 2020.

[58] J. Tian, Q. Liu, N. Cheng, A. M. Asiri, and X. Sun, "Self-supported Cu$_3$P nanowire arrays as integrated high-performance three-dimensional cathode for generating hydrogen from water," *Angewandte Chemie International Edition*, vol. 53, no. 36, pp. 9731–9735, 2014.

[59] Y. Guo, R. Khatoon, J. Lu et al., "Regulating adsorption ability toward polysulfides in a porous carbon/Cu$_3$P hybrid for an ultrastable high-temperature lithium-sulfur battery," *Carbon Energy*, vol. 3, no. 6, pp. 841–855, 2021.

[60] Y.-S. Lee and K.-S. Ryu, "Study of the lithium diffusion properties and high rate performance of TiNb$_6$O$_{17}$ as an anode in lithium secondary battery," *Scientific Reports*, vol. 7, no. 1, p. 16617, 2017.

[61] Y.-F. Xia, P. Guo, J.-Z. Li et al., "How to appropriately assess the oxygen reduction reaction activity of platinum group metal catalysts with rotating disk electrode," *iScience*, vol. 24, no. 9, article 103024, 2021.

[62] M. A. Patel, F. Luo, M. R. Khoshi et al., "P-doped porous carbon as metal free catalysts for selective aerobic oxidation with an unexpected mechanism," *ACS Nano*, vol. 10, no. 2, pp. 2305–2315, 2016.

[63] Q. He, J. Li, Y. Qiao, S. Zhan, and F. Zhou, "Investigation of two-electron ORR pathway of non-metallic carbon-based catalysts with P-C bond structure in Cl$^-$-bearing electrolytes," *Applied Catalysis B: Environmental*, vol. 339, p. 123087, 2023.

[64] M.-C. Sung, G.-H. Lee, and D.-W. Kim, "Kinetic insight into perovskite La0.8Sr0.2VO3 nanofibers as an efficient electrocatalytic cathode for high-rate Li-O$_2$ batteries," *InfoMat*, vol. 3, no. 11, pp. 1295–1310, 2021.

[65] A. Kondori, M. Esmaeilirad, A. M. Harzandi et al., "A room temperature rechargeable Li$_2$O-based lithium-air battery enabled by a solid electrolyte," *Science*, vol. 379, no. 6631, pp. 499–505, 2023.

[66] Y. Qiao, K. Jiang, H. Deng, and H. Zhou, "A high-energy-density and long-life lithium-ion battery via reversible oxide-peroxide conversion," *Nature Catalysis*, vol. 2, no. 11, pp. 1035–1044, 2019.

[67] D. Aurbach, B. D. McCloskey, L. F. Nazar, and P. G. Bruce, "Advances in understanding mechanisms underpinning lithium-air batteries," *Nature Energy*, vol. 1, no. 9, p. 16128, 2016.

[68] M. H. Brooker and J. B. Bates, "Raman and infrared spectral studies of anhydrous Li$_2$CO$_3$ and Na$_2$CO$_3$," *The Journal of Chemical Physics*, vol. 54, no. 11, pp. 4788–4796, 1971.